

# Describing material behavior of 3D-printed hollow elastomer hemispheres using uni-axial test data

By

Z.Z. van Hijfte

in partial fulfilment of the requirements for the degree of

**Master of Science**  
in Mechanical Engineering

at the Delft University of Technology,  
to be defended publicly on Monday March 27, 2023 at 14:00 PM.

Supervisors: Prof. dr. ir. H. Vallery  
Dr. ir. M.C. Rozendaal

Thesis committee: Prof. dr. ir. H. Vallery, TU Delft  
Dr. ir. M.C. Rozendaal, TU Delft  
Dr. ir. A.H.A. Stienen, TU Delft

*This thesis is confidential and cannot be made public until March 26, 2023.*

An electronic version of this thesis is available at <http://repository.tudelft.nl/>.

# Describing material behavior of 3D-printed hollow elastomer hemispheres using uni-axial test data

Zasha van Hijfte

**Abstract**—This thesis investigates the behavior of an elastomer spherical structure compressed by a small object compared to the cross-section of the structure. The study is based on the situation in which a child catches a ball multiple times with two hands. This was simplified to a situation where a hemisphere was cyclically compressed by a small object. The elastomer chosen was the cured resin Elastic 50A, which is manufactured by *Formlabs*. Stereo lithography was used to print the investigated structures. Layer-by-layer printing introduced the ability to print the same structure with different layering. Elastomers and rubbers cannot be described by a linear material model. Therefore, the non-linear behavior of the elastomer was obtained experimentally. Material behavior was described by performing a uni-axial tensile test with dumbbell specimens printed in three different directions according to ASTM D412. The dumbbell specimens were printed in the x-, y- and z-directions, representing upright, lateral and supine positions. A comparison between the specimen force-deflection responses and the finite-element analysis(FEA) responses showed that different models performed best for different print directions. *Ansys Mechanical* was used to calibrate the hyper-elastic material models available to describe a material with a single uni-axial test. The curve fitting tool of *Ansys* was used to acquire the Arruda-Boyce, Gent and Yeoh model constants. The 2nd-order Yeoh model performed best for the x-direction printed specimen. The 1st-order Yeoh model performed best for the y- and z-direction printed specimen. These models were used in the finite-element analysis on the elastomer hemispheres. The hemispheres were printed in the y- and z-direction, representing the upright and lateral positions. The experimentally obtained peak forces for the z-direction printed hemisphere were 19.61 and 17.76 N for the velocities of 50 and 500 mm/min, respectively. The peak forces for the y-direction printed hemisphere were 19.40 and 17.51 N for the velocities of 50 and 500 mm/min, respectively. The prediction of the finite-element analysis showed a higher peak force at 50 mm/min of 33.78, 29 and 36.27 N for the x-, y- and z-direction models used, respectively. The prediction of the finite-element analysis showed a higher peak force at 500 mm/min of 33.62, 28.91 and 36.1 N for the x-, y- and z-direction models used, respectively. The hysteresis found during the compression test did not match the hysteresis found in the FEA. The experimentally obtained hysteresis was larger than the hysteresis predicted by finite-element analysis. Both hemispheres were able to support the loads without damage for ten cycles.

**Keywords**— 3D-printing, Stereo lithography(SLA) , elastomer hemisphere, tensile test, resin, hysteresis, strain energy density model

## I. INTRODUCTION

Learning motor skills is an important part of children's development. Coordination of movements is an essential part of daily life [1]. A child's ability to interact with their environment, explore and manipulate objects and learn new skills depends on the quality of motor skills they develop [2] [3]. A coordinating task involves posture and the movement of the body. Some children are born premature, with very low birth weight or with a disability such as cerebral palsy

The author is with the Faculty of Mechanical, Maritime and Materials Engineering, Delft University of Technology (z.z.vanhijfte@student.tudelft.nl)

[4]. In 2008, 7.4 % of 175000 children in the Netherlands were born prematurely [5]. Half of preterm infants experience mild or moderate motor impairments [6]. They experience difficulties in balancing, gross and fine motor skills, manual dexterity and ball skills [7]. These types of motor skills can be achieved by participating in manipulative play. Manipulative play involves controlling an object with their body or body parts [8]. This type of play consists of elements such as catching, rolling, reaching, throwing, taking, carrying and collecting. A ball is a good candidate to aid children with training their manipulative skills.

One project, around the concept of a robot ball for children, uses a prototype called "Fizzy". Fizzy should feel like a pet friend to the children. Therefore, it must be able to move itself around and interact with the child. This autonomous behavior should be able to adapt to the specific child. In this way, the ball can tease children and get them excited to play. The target audience are children from two to seven years old. They should be able to play unrestricted with their ball.

Previous studies for project Fizzy investigated the role of the child's environment on physical activity due to play [2], [3]. One study compared two design interventions with two exercise-based interventions. The other investigates design strategies that promote bodily, dispersed and free play. An early prototype of Fizzy was used in this study to investigate these occurrences of the types of play. Another prior study used the same early prototype of Fizzy. This study investigated the object-with-intent in the human-computer interaction with Fizzy [9]. The study showed that Fizzy is able to motivate children to participate in physical activity.

The spherical design must enable the mentioned characteristics. The manufacturing of complex hollow spherical structures, which allow the placement and suspension of a drive system, is not possible with conventional manufacturing techniques [10], [11]. Additive manufacturing allows engineers to create complex hollow designs [10], [12]. It offers an alternative to conventional manufacturing methods by printing the structures layer-by-layer [13], [14]. The layers-by-layer build up allows for cavities within a structure. The cavities are bound by the limitations of 3D-printing. The structures are constrained by an overhang angle of  $45^\circ$  [15]. Printing lower overhang angles leads to sagging, because the structure is not able to hold its own weight [16]. A sphere has only one point of contact with a connecting flat surface. The printing angles around the point of contact are far lower than  $45^\circ$ . Therefore, support structure is needed during the printing process to prevent the spherical structure from sagging and rotating.

Rapid prototyping techniques like fused deposition modelling(FDM), material jetting(MJ), stereo lithography (SLA) and selective laser sintering(SLS) reduce the production time and costs [17], [18]. These different techniques used for 3D-printing have their benefits and disadvantages. A study by Ahn et al. showed that FDM 3D-printed parts with the material ABS showed anisotropic behavior [19]. The behavior was due to the printing pattern and the air gaps in between the extruded lines of filament. This caused the ASTM D638 dumbbell specimens to fail prematurely. Messimer et al. [20] studied the behavior of a specific type of thermoplastic polyurethane with ASTM D638 dumbbell specimens. They found that the behavior of the specimens depended on the printing direction. This indicates that fused deposition modelled designs can experience an-isotropic material behavior when printing soft plastics, which was confirmed by a study of Plott et al. [21]. A study by Mehdipour et al. [22]

showed that the base material polyamide 12 has almost isotropic and rate-independent behavior when manufactured with SLS and anisotropic and rate-dependent behavior compared with MJ. A study by Quintana et al. [23] investigated the effect of build direction on the mechanical behavior. They found that materials used for stereo lithography cannot be considered isotropic. A study by Wang et al. found that stereo lithography, compared to the other mentioned print technologies, has the highest molding precision and a faster printing speed [11].

The material for the ball must be sturdy and also flexible. Rubber-like materials, such as elastomers, exhibit those capabilities. Studies into elastomers found that they exhibit linear behavior at small strain and hyper-elastic behavior at larger deflections [24], [25]. Studies by Yildiz, Selvadurai et al. and Rezende et al. [26]–[28] determined the non-linear behavior of elastomers and natural rubber using only a uni-axial tensile test. The stress-strain response were used to determine the hyper-elastic material behavior. They were used to verify the compression of a rubber fender in the study by Yildiz [26], the behavior of an elastomer bearing pad in the study by Rezende et al. [28] and the behavior of a hyper-elastic membrane under pressure by Selvadurai et al. [27]. A study by Domingo-Roca et al. [29] used non-destructive material analysis with Flexible 50A resin. Their experiments were conducted with dynamic mechanical analysis to acquire the Young's modulus. The Young's modulus is not applicable when non-linear behavior emerges. A study by Von Steuben et al. [30] used Elastic 50A resin as material for needle penetration test. They were able to obtain linear elastic behavior for needle penetration.

This research investigates the force-deflection behavior of an elastic spherical structure. To do this, five major challenges were identified:

- The determination of the elastomer specimen behavior.
- The determination of the elastomer hemisphere behavior.
- The calibration of the hyper-elastic material model.
- Comparison of the tensile responses with finite-element analysis of the specimens.
- Comparison of the experimentally obtained behavior and the finite-element analysis of the hemispheres.

The elastomer behavior was determined by a uni-axial tensile test in multiple print directions. The behavior of elastomer hemispheres were obtained by a compression test. The responses from the tensile tests were calibrated with the calibration software of *Ansys Mechanical*. The obtained hyper elastic material models served as input for the finite-element analysis. Two sets of finite-element analysis were performed to obtain the behavior of the elastomer specimens and hemispheres. The results from the finite-element analysis were compared with the results from the experiments.

The second section discusses the steps to acquire the hyper-elastic material properties of an elastomer. This involves the performance of the tensile test according to ASTM D412 and the calibration of the strain energy density model. The next section discusses the elastomer hemisphere prototype. Here, the user-case and the compression test with unequal size surfaces are explained. The following section displays the two test setups. The first setup is the tensile test according to ASTM D412 and the second setup is about compressing the elastomer hemispheres. This section is followed by the results section. Here, the data of the tensile test is showed in stress-strain curves and two bar plots showing the ultimate tensile strength and the elongation at break. The data of the compression test is presented and put against the finite-element analysis. This section is followed by the discussion section on the results and the used methods. The last section will conclude on the research based on the results of the results and discussion on the conducted experiments.

## II. FABRICATION

### A. Overview of elastomer specimen

Two elastomer hemispheres were 3D-printed to investigate their force-deflection behavior. The two hemispheres were printed in two different direction. This allows the influence of print direction to

be determined for a hemisphere structure. When investigating an elastomer hemisphere design, it is important that the behavior of the CAD-model describes the prototype behavior. The choice of material influences the behavior of a structure. Therefore, the material properties were needed for the finite-element analysis. Rubber-like materials, such as elastomers, do not show a linear stress-strain response. The material behavior was calibrated by use of strain-energy density models. These models use elastomeric behavior, such as stress-strain responses, to predict the material behavior.

Fifteen dumbbell specimens were 3D-printed with the same elastomer as the hemispheres. They were printed in three different directions, which resulted in five specimens per direction. This allowed the influence of printing direction to be determined for the material used. The difference in behavior can then be related to the difference in behavior of the elastomer hemispheres. The force-deflection responses of the dumbbell specimens were obtained by a uni-axial tensile test. The force-deflection responses were used to obtain the stress-strain response of the specific print direction. Moreover, material properties can be related to those presented by the manufacturer.

### B. Stereo lithography (SLA)

The 3D-print method of stereo lithography was selected for this study. Stereo lithography uses liquid polymers, known as resins, to create a desired structure [31], [32]. This technique uses an ultra-violet(UV) laser to solidify the resin. The UV radiation causes a localized photo-polymerization process [31]. In the constrained surface approach, the structures are built upside down with the building platform suspended above the resin tank [32]. After a layer is cured, the platform was further pulled from the resin tank. After the structure is finished, it is washed and another curing step was performed at 60 ° Celsius for 20 minutes [33].

The support structure must be made from the same material as the structure [32]. It was not possible to use another material for the support structure because of the resin tank. The support structure is necessary for proper adhesion with the build platform because the bottom up printing approach must overcome the effects of gravity [32]. The placement of support structure is handled by a 3D-printing slicer program. This type of programs transforms the CAD-model into a 3D-printable file. The orientation of a desired structure influences the placement of the support structure [18]. Normally, support structures are printed with the support on less important parts of the desired structure.

### C. Dumbbell specimen

The material used for the dumbbell specimen is Elastic 50A. This material was a resin manufactured by *Formlabs*. The material properties, obtained by the resin manufacturer *Formlabs*, can be found in table I. The material properties were determined using experimental standards [33], [34]. The standard used was the one for uni-axial tensile testing of elastomers and rubbers, ASTM D412 [24], [35]. The resin was processed by photo-polymerization into the desired structure. Stereo lithography builds the structure layer-by-layer [31], [32]. The layering allowed for different solutions within a single structure.

The layer-by-layer printing of the structures allows for multiple printing directions of the specimens. The x-, y- and z-direction specified in figure 1 were used for the experiments. In this way, three different stress-strain responses were experimentally obtained. The use of specified print directions eliminated the possibility of redistribution of the support structure with the orientation of the part. The material properties by *Formlabs* did not specify the direction their specimen was printed. Therefore, the stress-strain response properties were compared against the data from *Formlabs*.

A stress-strain curve was not published by the manufacturer [33]. Therefore, the stress-strain response was obtained experimentally by performing a uni-axial tensile test. The behavior of non-rigid plastics can be tested by using ISO 37 [36], ASTM 638 [20] or

Property	Value	Test method
Density	1.02 gcm <sup>-3</sup>	-
Ultimate tensile strength	3.23 MPa	ASTM D412-A
Stress 50% elongation	0.94 MPa	ASTM D412-A
Stress 100% elongation	1.59 MPa	ASTM D412-A
Failure elongation	160 %	ASTM D412-A

TABLE I  
MATERIAL PROPERTIES OF ELASTIC 50A CURED RESIN [33], [34]

ASTM D412 [24], [37]. The manufacturer *Formlabs* used the ASTM D412 dimensions of die C to establish the properties of Elastic 50A [33]. Therefore, the dumbbell specimens used in this research were fabricated according to ASTM D412 die C. The specific dimensions of die C can be found in figure 1. The thickness specified by the standard was 2 mm.

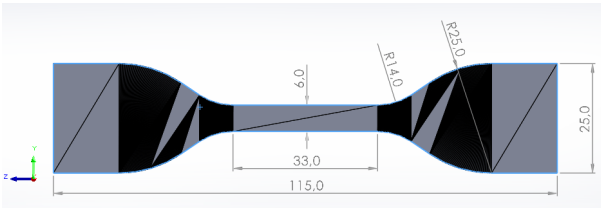


Fig. 1. Tensile test specimen according to ASTM D412 die C [35]

#### D. Elastomer hemisphere

The situation in which a child catches the ball with two hands was used in this study. This situation was simplified by taking a hemisphere pressed by a single hand. A study by Choi et al. found that the average hand area for Asian children in the age-group of seven to ten years was 71 cm<sup>2</sup> [38]. The found value had a deviation of 5.71 cm<sup>2</sup>. The study determined the surface area of the whole hand, excluding the fingers. Another study by Agarwal et al. [39] found an average hand surface area of Indian children of 85.646 cm<sup>2</sup> with a deviation of 21.1106 cm<sup>2</sup>. They also found the average palm area for the same group of children of 50.675 cm<sup>2</sup> with a deviation of 12.6026 cm<sup>2</sup>. The study was conducted with children in the age-group of two to seventeen years.

The current model of Fizzy has a diameter of 16 cm. Its cross-sectional area is 201.1 cm<sup>2</sup>. Both studies by Choi et al. and Agarwal et al. showed that the surface area of a child's hand is lower than the cross-sectional area of the sphere [38], [39]. Therefore, the experiment was conducted using a cylinder with a smaller radius compared to the hemisphere prototype. The cylinder represented the hand of a child pressing a ball. The compression cylinder of the universal testing machine (UTM) has a radius of 30 mm. The hemisphere prototype used, had a radius of 50 mm.

The elastomer hemisphere was also manufactured with Elastic 50A. The hemisphere was built in two different directions. The z-direction and the x- or y-direction. If we view a hemisphere in top view with the print direction on the vertical axis. A similar hemisphere can be made by printing the hemisphere horizontally and rotating it 90 degrees. Therefore, the hemisphere printed in x- or y-direction represented two printing directions. The thickness of the hemisphere was a free variable. It was taken the same as the thickness of the tensile specimens. This way, the results of the dumbbell specimens experiments were comparable to the results of the experiments with the hemisphere models.

### III. TEST SETUPS

#### A. Uni-axial tensile test

The tensile tests with the dumbbell specimen were performed in a controlled environment in accordance with the standard D412.

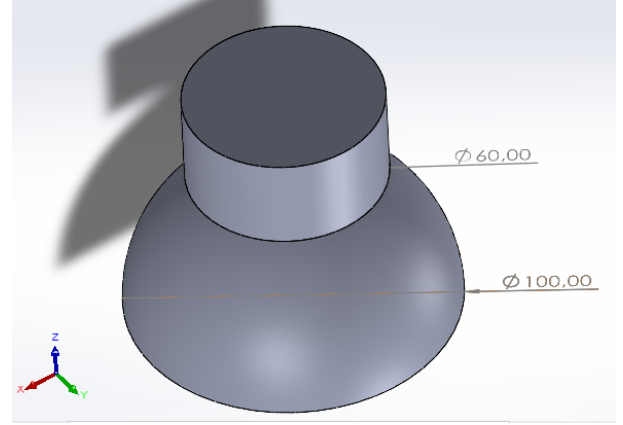


Fig. 2. Simplified model pressing ball

The standard specifies the setup, cross-head speed and temperature during testing [35]. The dumbbell specimens were printed according to the manufacturer's standard with a *Formlabs 3+* 3D-printer. The material behavior of the tensile specimens were determined by the *Zwick/Roell* universal testing machine with a 500 N loadcell. The testing machine was connected to a computer running the *Zwick/Roell* tensile test software. The setup can be found in figure 3. Before the tensile test, the thickness of each specimen was measured at three places according to ASTM D412 [35]. The first one at the top of the sample, the second one at the center of the sample and the third one at the bottom of the sample. The thickness measurements were performed by a *Heidenhain* gauge. The temperature during the experiments was recorded by an *EasyLog* EL-SIE-2. The temperature of the environment was kept between the limits of 21 °C and 25 °C. The cross head speed was set at 500 mm/min, which was consisted with the speed used by *Formlabs* [33]. The dumbbell specimens were manually clamped between two cross-heads. The preload was set to 0.5 N.

The tensile test produced a force-deflection curve. The stress [40] is determined by

$$\sigma = F/A. \quad (1)$$

Here, the stress  $\sigma$  is determined by the force  $F$  applied on the specimen and the surface  $A$  on which the force acts. The surface is the unstained surface of the specimen center [35]. The strain [40] is determined by

$$\epsilon = \frac{(L - L_0)}{L_0}. \quad (2)$$

Here, the strain  $\epsilon$  is determined by the initial length of the specimen  $L_0$  and the length after force application  $L$ . These two equations are used to create the stress-strain curve. This curve serves as input for the strain energy density model.

The maximum values of the acquired stress-strain curves were used to determine the ultimate tensile strength and the elongation at break. The mean value of the ultimate tensile strength and the elongation at break is determined by

$$\bar{\sigma} = \frac{\sum_i^n \sigma_i}{n}. \quad (3)$$

Here, the mean value  $\bar{\sigma}$  is determined by the measured stress value  $\sigma_i$  per specimen and the number of specimens used  $n$ . The stress response of the different specimens were compared by means of the standard deviation. The standard deviation [41] is determined by

$$S = \sqrt{\frac{\sum_i^n (\sigma_i - \bar{\sigma})^2}{n - 1}}. \quad (4)$$

Here, the standard deviation  $S$  is determined by the measured stress value  $\sigma_i$ , the average stress value  $\bar{\sigma}$  and the number of specimens used  $n$ .

The behavior of hyper-elastic materials, such as elastomers, can be described by a strain energy function. Therefore, the elastomer was assumed to behave incompressible, isotropic and reversible [25], [37]. The response with the most information on the stress-strain behavior was used for curve fitting the SED-models. The curve fitting was performed by *Ansys Mechanical*. The strain energy density functions of Arruda-Boyce, Gent and Yeoh were used for the calibration. These three models were described in Appendix A. The selection of the best fitting model was based on the capability of the calibrated curve to follow the stress-strain response. This was done by calculating the error between the two curves. The minimum value of the sum of squared error shows the most accurate fit [42]. *Ansys* determined the error with a normalized error [17]. This ensures that each data point gets equal weight. The normalized error [17] is determined by

$$E_{norm} = \left( \sum_{i=1}^n \frac{(\sigma_i^{pre} - \sigma_i^{exp})^2}{(\sigma_i^{exp})^2} \right)^{0.5}. \quad (5)$$

Here, the normalized error  $E_{norm}$  is determined by the predicted stress value  $\sigma_i^{pre}$ , the experimental stress value  $\sigma_i^{exp}$  and the number of specimens used  $n$ .

When different models have comparable error values, the model with the least amount of constants is considered optimal [42]. In addition, the calibration was also visually compared. The model must be able to follow the stress-strain response of the experimental data [42]. Furthermore, finite-element analysis was performed to compare the force-deflection predictions of the different models. The FEA was performed on the dumbbell specimens and compared with the experimental response.

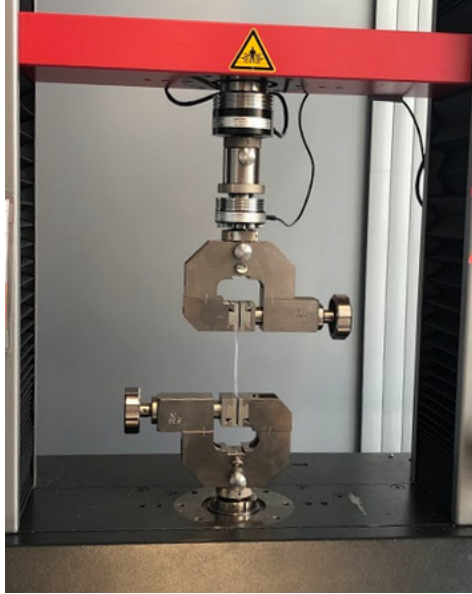


Fig. 3. Test setup tensile test

### B. Compression test with unequal size surfaces

The compression tests were performed with the elastomer hemispheres. The hemispheres were printed according to the manufacturer's standard with a *Formlabs 3+* 3D-printer. The force-deflection response of the elastomer hemispheres were obtained by the *Zwick/Roell* universal testing machine with a 500 N loadcell. The setup can be found in figure 4. The testing machine was connected to a computer running the *Zwick/Roell* cyclic compression software. The number of cycles was set to 10, to mimic the child catching a ball multiple times. The recorded force-deflection curves were stored in an excel-file. The thickness of the hemispheres were measured at four places. Each with a 90 degrees angle to the previous one.



Fig. 4. Test setup unequal surfaces compression

It was measured at the height of the location of maximum strain. The measurements were performed by a *Heidenhain* gauge. The temperature of the environment was recorded by an *EasyLog EL-SIE-2*. The temperature of the environment was kept between the limits of 21 °C and 25 °C. The compression speeds were set to 50 and 500 mm/min. The compression distances were set to 10, 20 and 30 mm. The hemispheres were centered on the disc. The upper cylinder was placed above the hemisphere before the start of the experiments. The cyclic compression was started when the cylinder detected a reaction force of the hemisphere when moving down from the start position.

During compression, a hemisphere expands laterally due to an increase in internal pressure [43]. The effect of air pressure difference will not be taken into account in this experiment. Therefore, ventilation holes were introduced in the compression setup. The holes served as a measure to equal the pressure inside the hemisphere with the outside pressure. The diameter of the cylinders and hemispheres were 60 mm and 100 mm, respectively. This allowed a gap at the bottom of 20 mm on each side of the sphere that provided space for ventilation holes. The gap was bridged by adding a disc to the bottom cylinder. It allowed support for the elastomer hemispheres and space for the ventilation holes. The design of the disc can be found in figure 5. The disc was cut out in the middle to fit over the lower cylinder of the universal testing machine. Therefore, the cut-out diameter was 60 mm with a depth of 2 mm. The disc was made with acrylonitrile butadiene styrene (ABS) filament with the 3D-printing technique fused deposition modelling. This printing method allowed for precise modelling of its features. The disc had eight holes with a diameter of 10 mm which centers lay on the 40 mm radius of the disc.

The finite-element analysis was performed by *Ansys Mechanical*. The software needed a friction coefficient for the contact between the hemisphere with its surroundings. Frictional behavior influences the behavior of a compressed structure. A friction coefficient for Elastic 50A was not documented. A study by Liu et al. [44] used a friction coefficient of 0.2 for a steel-rubber interface in *Ansys Mechanical*. Studies by Kunnil et al. and Li et al. [25], [45] used a friction coefficient of 0.3 for an elastomer-steel and rubber-plastic interface, respectively. Therefore, the coefficient of friction used in this study for finite-element analysis was set at 0.3.

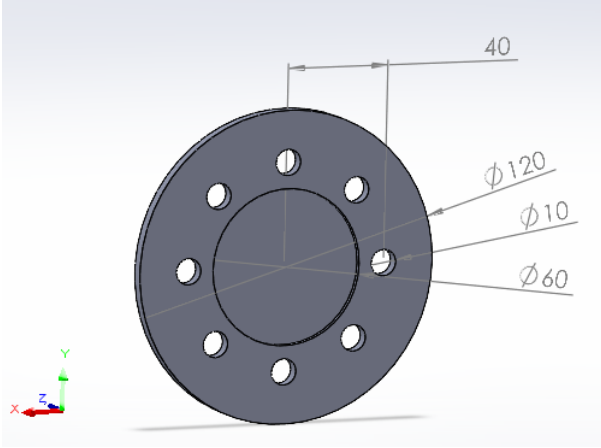


Fig. 5. Design of bottom plate with cut-out and ventilation holes

## IV. RESULTS

### A. Tensile testing Elastic 50A resin

The five specimens per built direction were produced and tested according to the ASTM D412. The specimens were manufactured by stereo lithography using a *Formlabs 3+* printer. The specimens built in the y- and z-direction were printed with support structure and were post-processed. The tensile specimen can be found in figure 6. The specimens printed in the y-direction, in the center of the figure, have the most support material remaining. Small pieces of support material were left on the specimen because it was expected that surface cuts from removing the support structure would reduce the ultimate tensile strength.

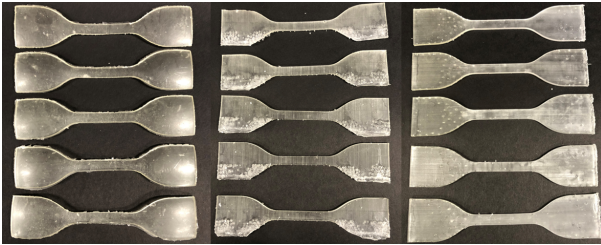


Fig. 6. Specimens before test, x-, y- and z-direction respectively

The thickness of the specimens was measured three times at three different locations, as the standard ASTM D412 prescribed. The thickness value of each specimen can be found in table III. The thickness and width of the center of each specimen were used to determine the ultimate tensile strength. The ultimate tensile strength with the standard deviation can be found in figure 11. The stress-strain curves for the different printing directions can be found in figures 7, 8 and 9. The pictogram in the left corner indicates the print direction with the arrow and the layering. The measured stress-strain responses follow a similar path for each of the built directions.

Specimen	X-Dir	Y-Dir	Z-Dir	
1	1.72	1.83	1.85	mm
2	1.72	1.82	1.82	mm
3	1.75	1.85	1.82	mm
4	1.75	1.84	1.81	mm
5	1.72	1.79	1.82	mm

TABLE II  
THICKNESS OF SPECIMENS PER DIRECTION

The standard deviation was also used to determine the average percentage of deviation between the stress-strain responses per built

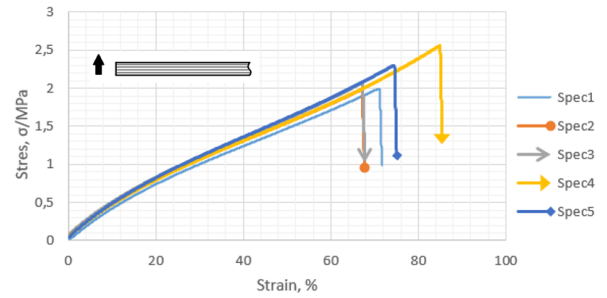


Fig. 7. Stress-strain curve specimens x-direction

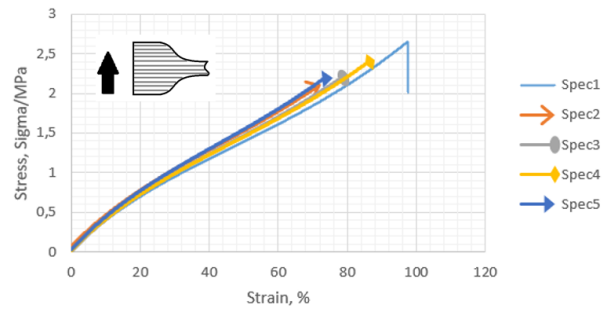


Fig. 8. Stress-strain curve specimens y-direction

direction. Therefore, the deviation was determined using values until 70% strain for the x- and y-directions and 60% strain for the z-direction. This ensured that all curves could be included. The average percentage of deviation can be found in table III. The highest deviation percentage was found for the specimens built in the x-direction and the lowest percentage was found for specimens built in the z-direction.

Direction	Percentage
X-Dir	5.41 %
Y-Dir	3.37 %
Z-Dir	2.90 %

TABLE III  
AVERAGE PERCENTAGE DEVIATION PER BUILT DIRECTION

The highest tensile strength is found in the z-direction. The lowest tensile strength is found in the specimens printed in the x-direction. Additionally, the largest deviation is found in the specimens built in the z-direction. All measured values of the ultimate tensile strength are lower than the comparative value of *Formlabs*. One of the stress-strain responses of figure 9 shows a larger ultimate tensile strength than the comparative value by *Formlabs*. This was also captured by the deviation of the z-direction printed specimen in figure 11. The deviation of the z-direction built specimens is the largest compared to the other directions.

Another value that was compared was the elongation at break. The tensile specimens fractured at a certain strain percentage. The average percentage of elongation at break per built direction can be found in figure 12. The largest strain at break was found in specimens built in the z-direction. The lowest strain at break was found in the x-direction. Also, the highest deviation was found in the specimens built in the z-direction. The values for the elongation at break for all directions were lower than the comparative value of *Formlabs*. None of the specimens tested could endure a strain percentage close to 160 %.

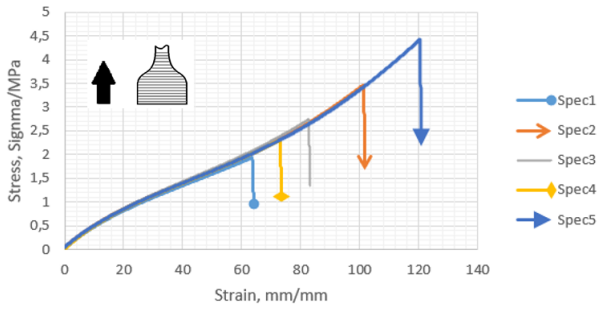


Fig. 9. Stress-strain curve specimens z-direction

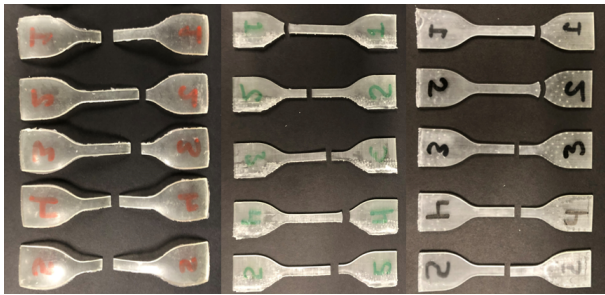


Fig. 10. Specimens after test, x-, y- and z-direction

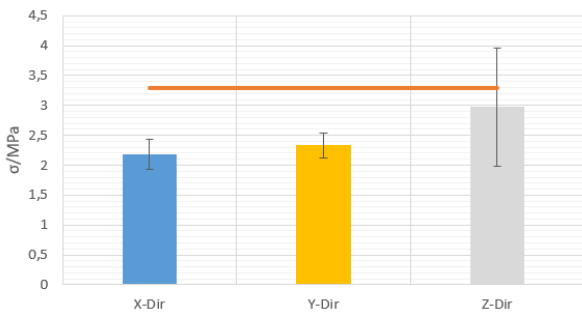


Fig. 11. Ultimate tensile strength per print direction

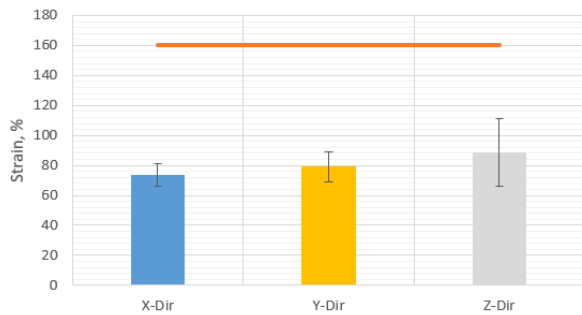


Fig. 12. Elongation at break per print direction

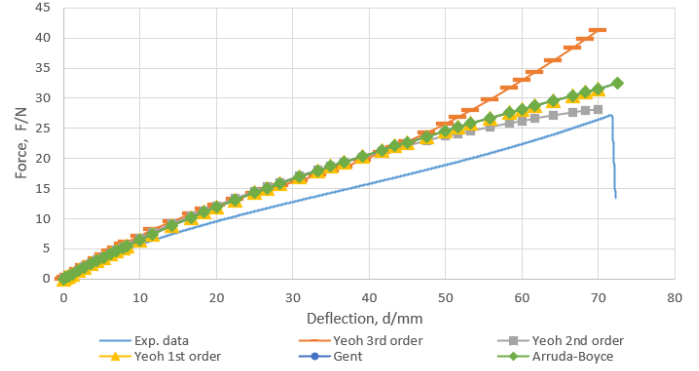


Fig. 13. Hyper-elastic curves of specimen built in x-direction.

### B. Calibration of strain energy density model

The calibrations were performed in order to obtain the material behavior of non-linear material Elastic 50A. The calibration of the strain energy density model was performed by the curve fitting tool of *Ansys Mechanical*. The CAD-model for the calibration used an updated thickness value based on the averages of the values found in table III. The Arruda-Boyce, Gent, Yeoh were the strain energy density models used for calibration. The calibrated values of the SED-constants can be found in appendix B. The normalized error values of the calibrations can be found in table IV. All normalized errors found for the three specimens were in the same order of magnitude, except for the Gent model in the y- and z-direction. The lowest error was found for the 3rd-order Yeoh model. The highest error values were found for the Gent model with the y- and z-direction printed specimens. For the specimens built in the x-direction the error values were similar. Increasing the order of the Yeoh model reduced the normalized error for all specimens.

The predictions of the hyper-elastic models and the experimental force-deflection responses of the dumbbell specimens can be found in figure 13, 14 and 15. The Arruda-Boyce, Gent and Yeoh 1st-order responses were similar in figure 13. The 3rd-order Yeoh model was able to capture the inflection point of the experimental force-deflection response. The Arruda-Boyce response was not present in figure 14, because the curve fitted solution was unstable. The Gent response predicts forces close to zero for the y-direction built specimen. The 1st- and 2nd-order Yeoh responses follow a similar pattern until 50 mm deflection. Then the force values increase because the 3rd-order Yeoh response captured the inflection point. The Gent response in figure 15 was again not able to follow the experimental force-deflection response and moved towards an asymptote around 75 mm deflection. The Arruda-Boyce and Yeoh responses follow a similar pattern until 70 mm deflection. Here again the 3rd-order Yeoh response is increasing because it captured the inflection point.

Model	X-Dir	Y-Dir	Z-Dir
Arruda-Boyce	8.43	5.69	9.89
Gent	8.43	685.8	613.9
Yeoh 1st	8.43	5.73	11.96
Yeoh 2nd	8.12	5.69	10.22
Yeoh 3rd	6.41	4.25	7.16

TABLE IV  
NORMALIZED ERROR PER STRAIN ENERGY DENSITY MODEL

### C. Cyclic compression hemisphere

The two elastomer hemispheres were printed with the same settings used for the dumbbell specimen. The printed structures can be found in figure 16 and figure 17. The indication of the layering can be found

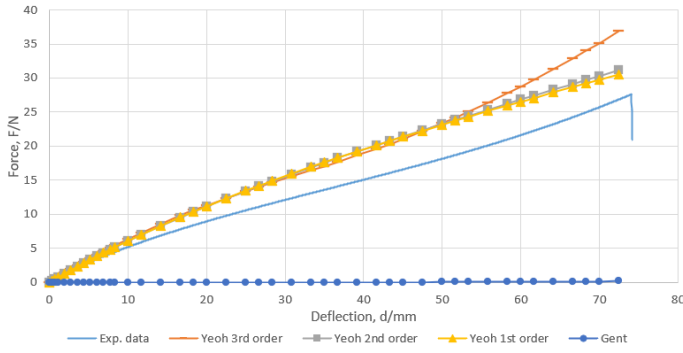


Fig. 14. Hyper-elastic curves of specimen built in y-direction.

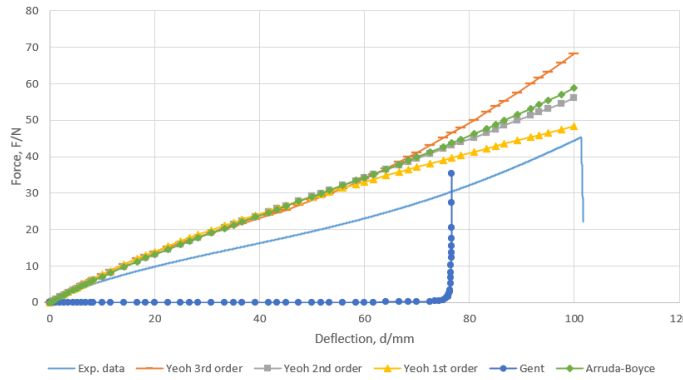


Fig. 15. Hyper-elastic curves of specimen built in z-direction.

bottom center and top center, respectively. Both hemispheres were post-processed to remove the support structure. The spots visible in both figures represent the attachment points of the support structure. The finite-element analysis on the hemispheres was performed by *Ansys Mechanical*. The thickness measurements on the hemispheres can be found in table [V](#). The FEA on the hemispheres used a CAD-model with a corrected thickness of 1.8 mm for both models. The 1st- and 2nd-order Yeoh models were used to perform the FEA. The top cylinder was constrained for all rotations and two translations. The cylinder could only move in the z-direction. The bottom surface of the ABS-disc was fully constrained. The number of elements used for the analysis was 5,398 with 4,570 nodes. The mesh was created to perform a non-linear analysis which allowed for large deflections in the calculations.

The force-deflection responses of the elastomer hemisphere were measured for two different velocities with three different deformations. This resulted in five sets of results for the xy-direction printed hemisphere, the z-direction printed hemisphere, the x-direction FEA, the y-direction FEA and the z-direction FEA. The experimental responses of the two hemispheres can be found in figures [20](#), [21](#), [25](#) and [26](#). All curves with a deformation of more than 10 mm showed a peak in measured force between the deformation values of 10 and 15 mm. Both print directions showed similar shaped graphs, a mountain-like shape when considering all curves together. The xy-direction printed hemisphere show a phase with a constant force around 5 mm deflection. All individual curves showed that the force-deflection response repeats itself each cycle. The peak forces for the z-direction printed hemisphere were 19.61 N and 17.76 N for the velocities of 50 and 500 mm/min, respectively. The peak forces for the y-direction printed hemisphere were 19.40 N and 17.51 N for the velocities of 50 and 500 mm/min, respectively. The hysteresis is higher for the responses with 500 mm/min with respect to the 50 mm/min.



Fig. 16. Hemisphere printed in x/y-direction

The force-deflection responses of the finite-element analysis can be found in figures [22](#), [23](#), [24](#), [27](#), [28](#) and [29](#). The peak force of all the FEA responses is also between the deformation values of 10 and 15 mm. The shapes for similar velocity responses were comparable. The peak force of the FEA in the z-direction was higher than the peak force in the x- and y-direction. The hysteresis found is similar for is similar per velocity. The hysteresis between velocity differs on certain points. The curves for 20 and 30 mm deformation with a velocity of 500 mm/min showed rounded peaks. The same responses with a velocity of 50 mm/min have dented peaks. The FEA predictions showed a higher peak force at 50 mm/min of 33.78 N, 29 N and 36.27 N for the x-, y- and z-direction models used, respectively. The FEA prediction also showed a higher peak force at 500 mm/min of 33.62 N, 28.91 N and 36.1 N for the x-, y- and z-direction models used, respectively. The FEA with 50 mm/min showed more hysteresis in the region between 0 and 12 mm deflection.

Location	XY-Dir	Z-Dir	
0°	1.76	1.78	mm
90°	1.79	1.85	mm
180°	1.82	1.77	mm
270°	1.82	1.81	mm

TABLE V  
THICKNESS MEASUREMENTS HEMISPHERES

The deformation behavior of the hemisphere was also obtained. The location of the highest strain values was determined by finite-element analysis on the hemisphere model and can be found in figure [18](#). The angle between the layers and the tangent line was estimated at the location of the highest strain. The angle between the tangent line and the ground was around 45°. This tangent line was also at a similar angle to both print directions of the hemispheres. Singular deformation data of the elastomer hemispheres can be found in figure [19](#). Here, the deformation for 10, 20 and 30 mm was shown. This is compared against the deformation of the FEA, which is also found in figure [19](#). The FEA deformation was shown in a cut-trough. In this way, the internal behavior of the hemisphere was shown. The elastomer hemisphere were not clear enough to confirm the predicted deformation pattern.

## V. DISCUSSION

### A. Performance of the tensile specimen

When comparing the ultimate tensile strength and the elongation at break of the specimens with the values presented by *Formlabs*, the

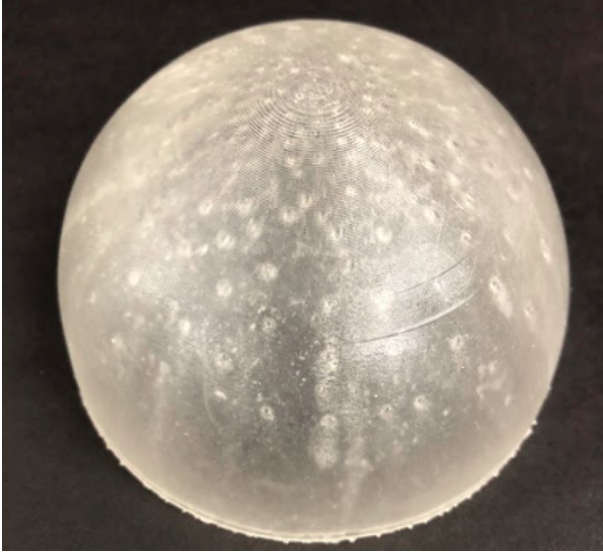


Fig. 17. Hemisphere printed in z-direction

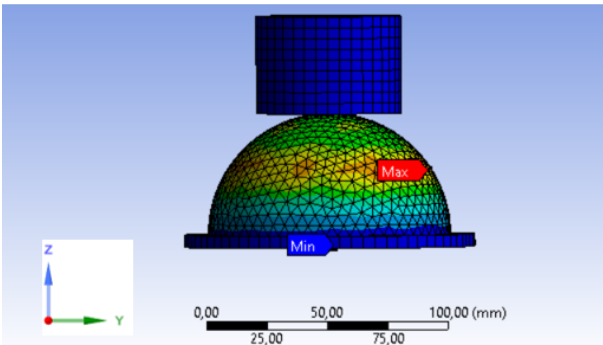


Fig. 18. Location of maximum strain hemisphere

average values found for the ultimate tensile strength and elongation at break were lower than the comparative values. There was a difference found of more than 0.6 MPa between the ultimate tensile strength for the z-direction against the x- and y-directions. This difference could be explained by the difference in print direction. The specimens built in the z-direction were elongated orthogonal to the layering, while the specimens built in the x- and y-direction were elongated parallel to the build direction. The z-direction built specimen were closest to the comparative value, with a difference of

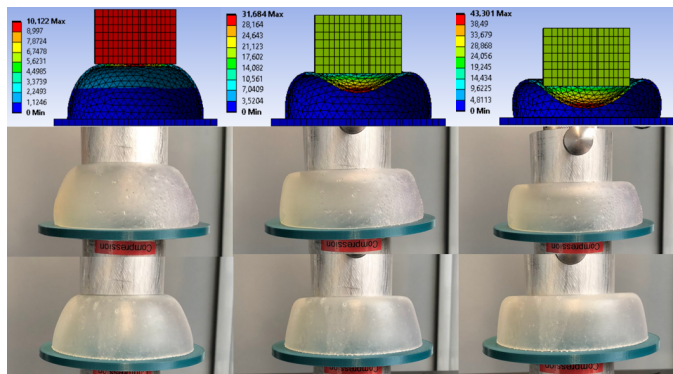


Fig. 19. Deformation of hemisphere FEA(top), xy-direction(middle) and z-direction(bottom)

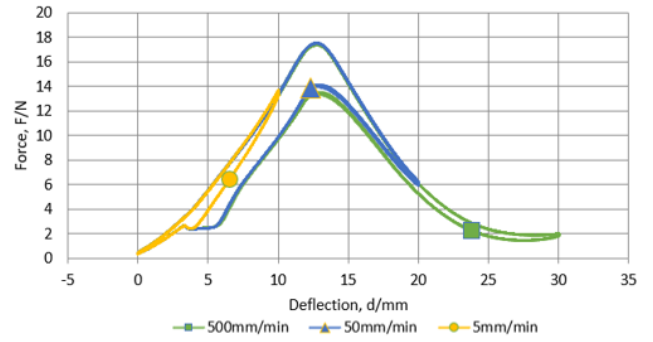


Fig. 20. Force-deflection curve XY-direction 50mm/min

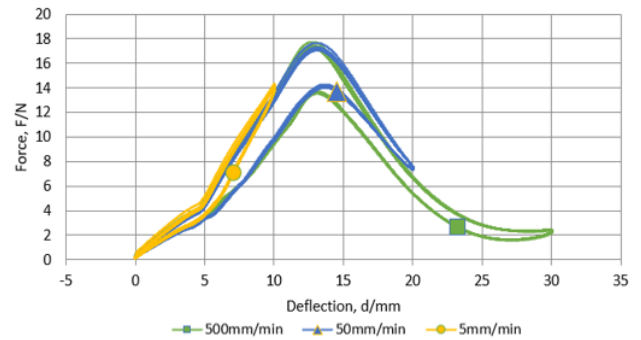


Fig. 21. Force-deflection curve Z-direction 50mm/min

0.32 MPa. One of the stress-strain responses showed a higher value for the ultimate tensile strength it reached 4.42 MPa. This shows that only the z-direction built specimen were capable of achieving the comparative value. This suggests that the print direction used by *Formlabs* was the z-direction.

The values found for the elongation at break were all around 50% lower than the comparative value. The smallest difference found was 71.3% for the specimens built in the z-direction. The difference could be explained by the remains and removal of the support structure. The cuts made for the removal of the support structure could influence the performance of the tensile specimen. On the contrary, the specimens built in the x-direction were not affected by the removal of support structure. As seen in figure 10 the specimens all break in the middle section of the specimen. Some of the specimen in the y- and z-direction do not break in the middle section. Therefore, the cuts made to remove the support structure could impact the location of the break but it does not explain the difference.

There was also a difference between the dimensions send to the *Formlabs* 3+ 3D-printer. The thickness of the model was specified to be 2 mm. The difference in thickness was greatest for the specimen built in the x-direction. The data by *Formlabs* specified that the dimensions of ASTM D412 were used. The difference in elongation could be the explanation for the difference in thickness. The measured thickness of the specimen was used for the finite-element analysis of the specimens.

### B. Calibration of strain energy density model

A single stress-strain response was used to calibrate the SED-models. The stress-strain experiments were performed with the standard ASTM D412. This ensured that the stress-strain curves can be compared. The stress-strain responses found in figures 7, 8 and 9 show similar curves. The similarity was proven by the average percentage of deviation found in table III. The largest

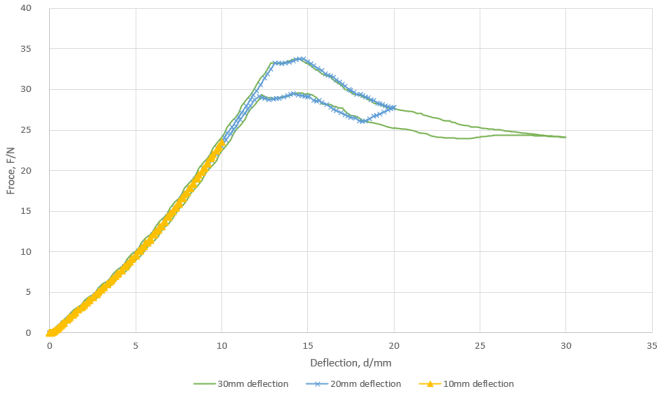


Fig. 22. Force-deflection curve FEA X-direction 50mm/min

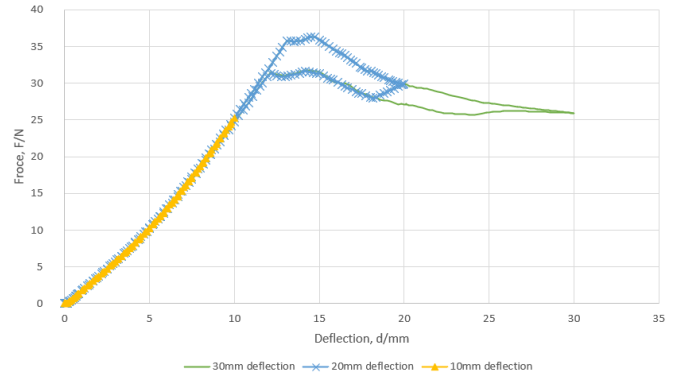


Fig. 24. Force-deflection curve FEA Z-direction 50mm/min

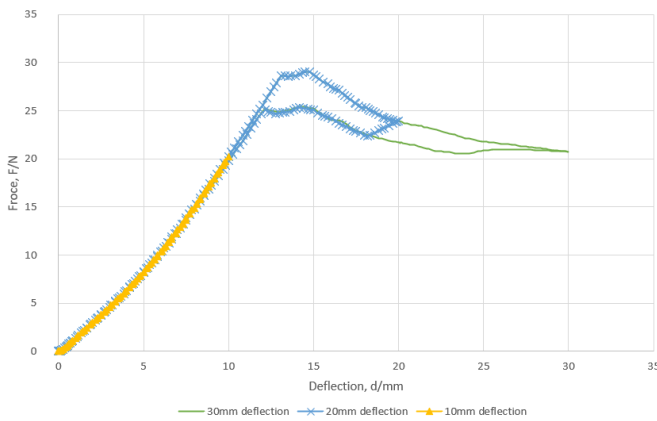


Fig. 23. Force-deflection curve FEA Y-direction 50mm/min

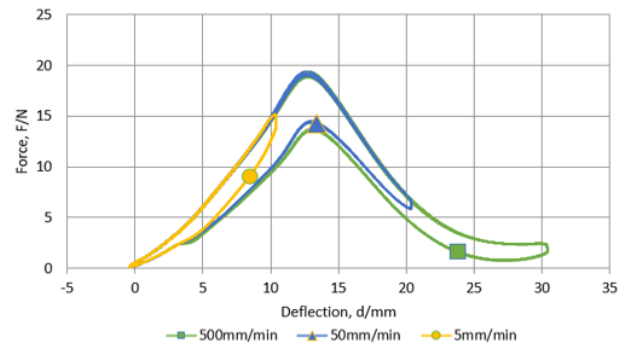


Fig. 25. Force-deflection curve XY-direction at 500mm/min

percentage found was 5.41 %, this was for specimens printed in the x-direction. The expected tensile values for the elastomer hemispheres are unknown. Therefore, and because of comparability, the response with the most stress-strain performance data was used for calibration.

The SED-models used for calibration were based on the first strain-invariant. The calibrated SED-models were used for the FEA on the dumbbell specimens. Those FEA's were used to compare the hyper-elastic behavior of the tensile specimens against the force-deflection responses found with tensile testing. When the normalized error found in table IV were similar, the force-deflection responses in figures 13, 14 and 15 also showed similarity. This was the case for the Arruda-Boyce, Gent and Yeoh 1st-order model for the specimens built in the x-direction. The same occurs for the 1st- and 2nd-order Yeoh model for specimens built in the y-direction and the Arruda-Boyce and 2nd-order Yeoh model in the z-direction. The difference in normalized error was 0.04 and 0.33, respectively. The Gent-model prediction for the y- and z-direction built specimen found in figures 13 and 14 was not able to capture the experimental response. The normalized errors found for both directions also suggest that the model was not able to capture the experimental stress-strain response. The Yeoh models for the y- and z-direction show that a decrease in normalized error results in an increase in the force-deflection response. This was not expected, because the lowest normalized error suggests that it was the best predicting model [42].

The Yeoh 3rd-order responses were the only predictions which were able to capture the inflection point of the experimental response. The other curves did not have an inflection point. According to the study by Gorash et al. [42], the model with the best s-shape and lowest error should be used for finite-element analysis of the structure. This suggested that Yeoh's 3rd-order model must be used for further analysis. In contrast, the estimated force around the largest

deflections has the largest offset with Yeoh's 3rd-order response. The model with the closest predictions for large strains were the Yeoh 2nd-order for the x-direction and the Yeoh 1st-order for the y- and z-direction. In addition, according to Selvadurai et al. [27] the simplest model that matches the forces best must be selected. This argument supports for the lower order Yeoh models. Therefore, these models are used for the analysis of the hemispheres.

### C. Experimental vs. FEA behavior

The SED-models were calibrated with only a uni-axial test. This was allowed when using the Arruda-Boyce, Gent and Yeoh models. The FEA responses do not match the experimental responses. There was a negligible amount of hysteresis found for the first 12 mm of deflection in the FEA responses. Moreover, the peak forces found in the FEA were higher and the decrease in force after the peak value was less steep. The curves decrease to a constant value around 18 N for the x-direction and 21 N for the y- and z-direction. It was unfortunate that the elastomer hemispheres are not fully transparent. Therefore, the deformation pattern of the FEA cannot be compared against the deformation of the elastomer model. The deformation pattern could give an explanation for the difference in the force drop after the peak.

The deformation found for the different print directions of the hemisphere in figure 19 matched the deformation pattern of the prediction of the FEA first two cases. In the third case, with 30 mm deformation, the FEA predictions showed convex shaped at both sides. This could indicate that more force was needed to arrive at that level of deflection.

Additionally, the deformation velocity of the hemisphere models had a different direction than the elongation velocity of the dumbbell specimens. The deformation velocity of the compression cylinder was set similar to the elongation velocity. The cyclic experimental tests

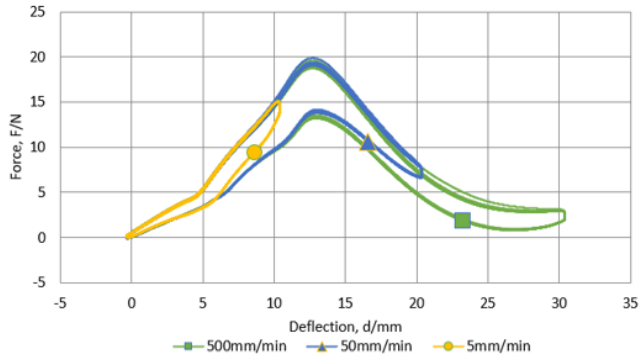


Fig. 26. Force-deflection curve Z-direction at 500mm/min

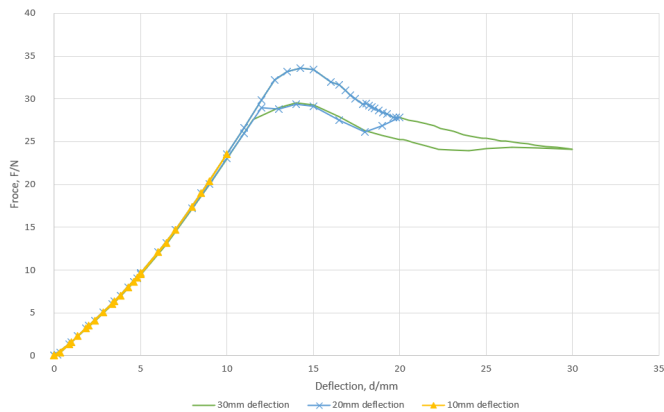


Fig. 27. Force-deflection curve FEA X-direction 500mm/min

showed that Elastic 50A had repeatedly followed the previous curve. Therefore, the structure does not experience plastic deformation. This would have caused an increase in hysteresis. An increase in deformation velocity did cause an increase in hysteresis. Those effects were not found in the FEA on the hemispheres. It was assumed that the strain velocity of the elements of the hemisphere, at the location of highest strain, were larger than the compression velocity of the cylinder. Therefore, the velocities used can not be taken as the strain velocity of the hemispheres.

The matching of the tensile specimen with the print directions was estimated by taking the location of maximum strain. This location defined a height for which the layering is similar. This was the case for the z-direction printed hemisphere. The xy-direction printed hemisphere was dissimilar at the cross-section for the same height. The tangent line with the location of maximum strain was taken as the direction. This direction has an angle on the layering of both hemispheres. Therefore, there was no direct match between the dumbbell specimen and the hemispheres.

The FEA force-deflection curves predicted each a different peak force. The highest was found for the x-direction and the lowest was found for the y-direction. This would suggest that, since all the prediction were higher than the experimental peak force value, that the y-direction is the best predictor. On the contrary, the results from the tensile test showed that the layering of a dumbbell specimen influences the force deflection behavior. Therefore, it was impossible to claim that the y-direction FEA was the best prediction.

The effect of thickness differences between the CAD-models and the dumbbell specimens and hemispheres could have caused the difference in force values found. The thickness was corrected for the dumbbell specimens, because lower values were found for the thickness. Therefore, this could indicate that the other dimensions did also not match with the ASTM D412 die C specifications. The same

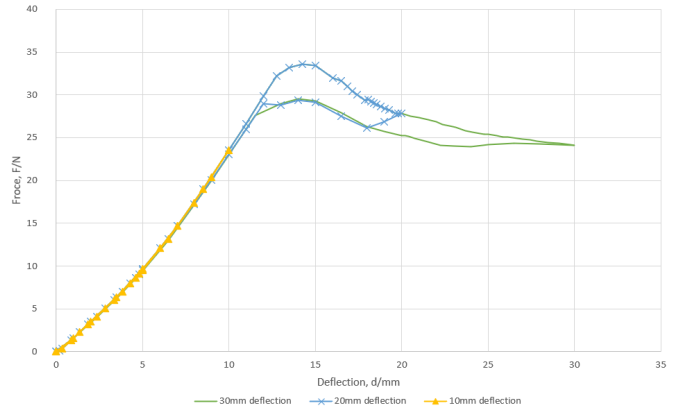


Fig. 28. Force-deflection curve FEA Y-direction 500mm/min

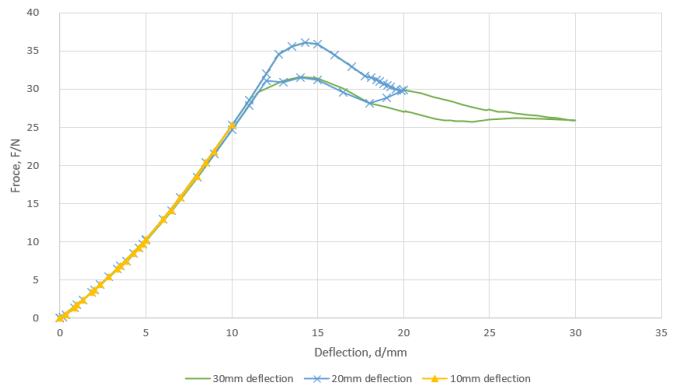


Fig. 29. Force-deflection curve FEA Z-direction 500mm/min

holds for the hemisphere models. The differences in thickness could explain that higher values found in the FEA's of the hemispheres. However, this did not explain the difference is declining angle after the peak force in the force-deflection behavior.

#### D. Future work

The following suggestions are made for future work. First, the printing method accuracy of acquiring structures with the specified dimensions could be investigated. This would ensure that the dimensions of the CAD-model match with the printed structure. Second, when the first suggestion does not deliver the sought solution, the hyper-elastic behavior of Elastic 50A could be further investigated. To do this, the bi-axial tension response and pure shear should be investigated and added in the calibration process. This would ensure that the Mooney-Rivlin, Ogden, Polynomial and Extended tube models could be used together with the model used in this research. Third, a study could be conducted on finding the friction coefficient of Elastic 50A to increase the probability of obtaining a matching FEA. Finally, a study into the effect of air pressure in a closed elastomer ball could be conducted.

## VI. CONCLUSION

The feasibility of describing the hyper-elastic behavior of elastomer hemispheres by use of calibrating a strain energy density model on a uni-axial test has been demonstrated. The material properties of Elastic 50A were not verified by the uni-axial tensile test of this study. The ultimate tensile strength of the specimens printed in the z-direction were comparable. By contrast, the values found for the elongation at break were around 50% lower.

The 2nd-order Yeoh model had the closest force-deflection prediction for x-direction printed specimens. The 1st-order Yeoh model had the closest force-deflection prediction for the y- and z-direction printed specimens. The 3rd-order Yeoh model was the only model that incorporated an inflection point in the force-deflection prediction. All models, except the Gent model for the y- and z-direction predicted a higher force than the experimental response.

The force-deflection behavior cannot be described by SED-models calibrated with on uni-axial tensile test. The FEA-responses predicted larger forces than the experimentally obtained responses. The model that predicted the lowest force was the model that used the data from the specimen printed in y-direction. The model was the 1st-order Yeoh model. Moreover, the amount of hysteresis found in the FEA was lower than the experimentally observed hysteresis. The force-deflection curves on the hemisphere prototypes did confirm the repeatability. Therefore, both hemispheres were able to support the loads without damage for ten cycles. Exceeding the peak force of a ball made from Elastic 50A, neglecting the effects of air pressure, will result in both hands touching each other with two layers of the hemisphere in between.

#### ACKNOWLEDGMENTS

The author would like to thank the supervisors Heike Vallery and Marco Rozendaal for their guidance and support during my thesis. The author would also like to thank Spiridon van Veldhoven for helping with the manufacturing of the elastomer specimens and hemispheres. Finally, the author would like to thank Mascha Slingerland for her guidance with the test setup.

#### REFERENCES

- [1] J. Massion, A. Alexandrov, and A. Frolov, "Why and how are posture and movement coordinated?" *Progress in Brain Research*, vol. 143, pp. 13–27, 2004.
- [2] B. Boon, M. Rozendaal, M. Van den Heuvel-Eibrink, J. J. van der Net, M. van Grotel, and P. J. Stappers, "Design Strategies for Promoting Young Children's Physical Activity }A Playscapes Perspective," *International Journal of Design*, vol. 14, no. 3, pp. 1–18, 2020.
- [3] B. Boon, J. Van Der Net, M. Rozendaal, P. J. Stappers, and M. M. Van Den Heuvel-Eibrink, "Playscapes: A design perspective on young children's physical play," *Proceedings of IDC 2016 - The 15th International Conference on Interaction Design and Children*, pp. 181–189, 6 2016.
- [4] I. C. van Haastert, L. S. de Vries, P. J. Helders, and M. J. Jongmans, "Early gross motor development of preterm infants according to the Alberta Infant Motor Scale," *The Journal of Pediatrics*, vol. 149, no. 5, pp. 617–622, 11 2006.
- [5] J. Zeitlin, K. Szamotulska, N. Drewniak, A. D. Mohangoo, J. Chalmers, L. Sakkeus, L. Irgens, M. Gatt, M. Gissler, and B. Blondel, "Preterm birth time trends in Europe: a study of 19 countries," *BJOG : an international journal of obstetrics and gynaecology*, vol. 120, no. 11, pp. 1356–1365, 10 2013. [Online]. Available: <https://pubmed.ncbi.nlm.nih.gov/23700966/>
- [6] A. J. Spittle and J. Orton, "Cerebral palsy and developmental coordination disorder in children born preterm," *Seminars in Fetal and Neonatal Medicine*, vol. 19, no. 2, pp. 84–89, 4 2014. [Online]. Available: [http://www.sfnjournal.com/article/S1744165X13001145/fulltexthttp://www.sfnjournal.com/article/S1744165X13001145/abstracthttps://www.sfnjournal.com/article/S1744-165X\(13\)00114-5/abstract](http://www.sfnjournal.com/article/S1744165X13001145/fulltexthttp://www.sfnjournal.com/article/S1744165X13001145/abstracthttps://www.sfnjournal.com/article/S1744-165X(13)00114-5/abstract)
- [7] J. F. De Kieviet, J. P. Piek, C. S. Aarnoudse-Moens, and J. Oosterlaan, "Motor Development in Very Preterm and Very Low-Birth-Weight Children From Birth to Adolescence: A Meta-analysis," *JAMA*, vol. 302, no. 20, pp. 2235–2242, 11 2009. [Online]. Available: <https://jamanetwork.com/journals/jama/fullarticle/184952>
- [8] S. Rahaarjo, A. Wibowo, O. Andiana, Ibrahim, R. Pelana, R. Susiono, Sujarwo, R. Antoni, and E. F. Amalia, "Throw and catch the ball games for children with dyskinesia-type cerebral palsy to improve eye-hand coordination movements," *Journal of Physical Education and Sport*, vol. 21, pp. 2419–2424, 8 2021.
- [9] M. C. Rozendaal, B. Boon, and V. Kaptelinin, "Objects with Intent," *ACM Transactions on Computer-Human Interaction (TOCHI)*, vol. 26, no. 4, pp. 1–33, 6 2019. [Online]. Available: <https://dl.acm.org/doi/abs/10.1145/3325277>
- [10] T. Pereira, J. V. Kennedy, and J. Potgieter, "A comparison of traditional manufacturing vs additive manufacturing, the best method for the job," *Procedia Manufacturing*, vol. 30, pp. 11–18, 2019.
- [11] S. Wang, Y. Ma, Z. Deng, K. Zhang, and S. Dai, "Implementation of an elastoplastic constitutive model for 3D-printed materials fabricated by stereolithography," *Additive Manufacturing*, vol. 33, p. 101104, 5 2020.
- [12] J. ZHU, H. ZHOU, C. WANG, L. ZHOU, S. YUAN, and W. ZHANG, "A review of topology optimization for additive manufacturing: Status and challenges," *Chinese Journal of Aeronautics*, vol. 34, no. 1, pp. 91–110, 1 2021.
- [13] M. F. Ernst, A. Maletzko, S. Baumann, N. Baumann, C. Hübner, and C. Höhne, "FFF 3D Printing of Small Porous Structures from Polymer Compounds Using the Ultimaker 3," *Macromolecular Materials and Engineering*, p. 2200095, 8 2022. [Online]. Available: <https://onlinelibrary.wiley.com/doi/10.1002/mame.202200095>
- [14] S. Maurya, B. Malik, P. Sharma, A. Singh, and R. Chalisgaonkar, "Investigation of different parameters of cube printed using PLA by FDM 3D printer," *Materials Today: Proceedings*, vol. 64, pp. 1217–1222, 1 2022.
- [15] Y. Mass and O. Amir, "Topology optimization for additive manufacturing: Accounting for overhang limitations using a virtual skeleton," *Additive Manufacturing*, vol. 18, pp. 58–73, 12 2017.
- [16] M. Farhan Khan, A. Alam, M. Ateeb Siddiqui, M. Saad Alam, Y. Rafat, N. Salik, and I. Al-Saidan, "Real-time defect detection in 3D printing using machine learning," *Materials Today: Proceedings*, vol. 42, pp. 521–528, 2021.
- [17] D. Huri and T. Mankovits, "Comparison of the material models in rubber finite element analysis," *IOP Conference Series: Materials Science and Engineering*, vol. 393, p. 012018, 8 2018. [Online]. Available: <https://iopscience.iop.org/article/10.1088/1757-899X/393/1/012018>
- [18] D. T. Pham, S. S. Dimov, and R. S. Gault, "Part Orientation in Stereolithography," *The International Journal of Advanced Manufacturing Technology*, vol. 15, no. 9, pp. 674–682, 8 1999.
- [19] S. Ahn, M. Montero, D. Odell, S. Roundy, and P. K. Wright, "Anisotropic material properties of fused deposition modeling ABS," *Rapid Prototyping Journal*, vol. 8, no. 4, pp. 248–257, 10 2002. [Online]. Available: <https://www.emerald.com/insight/content/doi/10.1108/13552540210441166/full/html>
- [20] P. Messimer, B. OâToole, and M. Trabia, "Identification of the Mechanical Characteristics of 3D Printed NinjaFlex®," in *Volume 9: Mechanics of Solids, Structures, and Fluids*. American Society of Mechanical Engineers, 11 2019. [Online]. Available: <https://asmedigitalcollection.asme.org/IMECE/proceedings/IMECE2019/59469/Salt%20Lake%20City,%20Utah,%20USA/1073444>
- [21] J. Plott, X. Tian, and A. J. Shih, "Voids and tensile properties in extrusion-based additive manufacturing of moisture-cured silicone elastomer," *Additive Manufacturing*, vol. 22, pp. 606–617, 8 2018. [Online]. Available: <https://linkinghub.elsevier.com/retrieve/pii/S2214860417302804>
- [22] F. Mehdipour, U. Gebhardt, and M. Kästner, "Anisotropic and rate-dependent mechanical properties of 3D printed polyamide 12 - A comparison between selective laser sintering and multi jet fusion," *Results in Materials*, vol. 11, p. 100213, 9 2021. [Online]. Available: <https://linkinghub.elsevier.com/retrieve/pii/S2590048X21000467>
- [23] R. Quintana, J.-W. Choi, K. Puebla, and R. Wicker, "Effects of build orientation on tensile strength for stereolithography-manufactured ASTM D-638 type I specimens," *The International Journal of Advanced Manufacturing Technology*, vol. 46, no. 1-4, pp. 201–215, 1 2010.
- [24] M. R. Sheikhi, B. Shamsadinlo, Ä. Ünver, and S. Gürgen, "Finite element analysis of different material models for polyurethane elastomer using estimation data sets," *Journal of the Brazilian Society of Mechanical Sciences and Engineering*, vol. 43, no. 12, p. 554, 12 2021. [Online]. Available: <https://link.springer.com/10.1007/s40430-021-03279-9>
- [25] M. Kunnil, D. Yamarthi, and S. K. Kompally, "Finite Element Analysis of Elastomers Using ANSYS," in *Volume 2: Plant Systems, Structures, and Components; Safety and Security; Next Generation Systems; Heat Exchangers and Cooling Systems*. American Society of Mechanical Engineers, 7 2012, pp. 75–82. [Online]. Available: <https://asmedigitalcollection.asme.org/ICONE/proceedings/ICONE20-POWER2012/44960/75/293227>
- [26] F. Yildiz, "The effect of different strain energy functions on rubber fender," *Journal of Elastomers & Plastics*, vol. 46, no. 8, pp. 722–736, 12 2014. [Online]. Available: <http://journals.sagepub.com/doi/10.1177/0095244313489912>
- [27] A. Selvadurai and M. Shi, "Fluid pressure loading of a hyperelastic membrane," *International Journal of Non-Linear Mechanics*, vol. 47,

- no. 2, pp. 228–239, 3 2012. [Online]. Available: <https://linkinghub.elsevier.com/retrieve/pii/S0020746211001193>
- [28] R. C. Rezende, M. Greco, and D. F. Lalo, “Numerical analysis of an elastomeric bearing pad by hyperelastic models,” *Revista de la construcción*, vol. 19, no. 3, pp. 301–310, 2020. [Online]. Available: <http://revistadelaconstruccion.uc.cl/index.php/RDLC/article/view/rdlc.19.3.301>
- [29] R. Domingo-Roca, L. Ascjak, J. F. C. Windmill, H. Mulvana, and J. C. Jackson-Camargo, “Non-destructive Analysis of the Mechanical Properties of 3D-Printed Materials,” *Journal of Nondestructive Evaluation*, vol. 41, no. 1, p. 22, 3 2022.
- [30] T. von Steuben, F. K. Enzmann, S. Spintzyk, F. Rupp, and A. Roehler, “Needle Penetration Simulation: Influence of Penetration Angle and Sample Stress on the Mechanical Behaviors of Polymers Applying a Cast Silicone and a 3D-Printed Resin,” *Materials*, vol. 15, no. 16, p. 5575, 8 2022.
- [31] J. Huang, Q. Qin, and J. Wang, “A Review of Stereolithography: Processes and Systems,” *Processes*, vol. 8, no. 9, p. 1138, 9 2020.
- [32] C. Schmidleithner and D. M. Kalaskar, “Stereolithography,” in *3D Printing*. InTech, 10 2018.
- [33] Formlabs, “Material Data Sheet Elastic 50A,” 2019. [Online]. Available: <https://formlabs-media.formlabs.com/datasheets/2001420-TDS-ENUS-0.pdf>
- [34] —, “Elastic 50A Resin Safety Data Sheet,” 2020. [Online]. Available: <https://dental-media.formlabs.com/datasheets/2001417-SDS-ENEU-0.pdf>
- [35] ASTM International, “ASTM D412: Standard Test Methods for Vulcanized Rubber and Thermoplastic Elastomers-Tension,” West Conshohocken, PA, Tech. Rep., 2021. [Online]. Available: <https://www.astm.org/d0412-16r21.html>
- [36] D. Re, F. De Angelis, G. Augusti, D. Augusti, S. Caputi, M. DâAmario, and C. DâArcangelo, “Mechanical Properties of Elastomeric Impression Materials: An In Vitro Comparison,” *International Journal of Dentistry*, vol. 2015, pp. 1–8, 2015.
- [37] D. Dos Santos, D. Carastan, L. Tavares, and G. Batalha, “Polymeric Materials Characterization and Modeling,” in *Comprehensive Materials Processing*. Elsevier, 2014, pp. 37–63. [Online]. Available: <https://linkinghub.elsevier.com/retrieve/pii/B9780080965321002053>
- [38] H. Choi, M. S. Park, and H.-M. Lee, “Hand surface area as a percentage of body surface area in Asian children: A pilot study,” *Burns*, vol. 37, no. 6, pp. 1062–1066, 9 2011.
- [39] P. Agarwal and S. Sahu, “Determination of hand and palm area as a ratio of body surface area in Indian population,” *Indian Journal of Plastic Surgery*, vol. 43, no. 1, p. 49, 2010.
- [40] S. M. Zayed, A. M. Alshimy, and A. E. Fahmy, “Effect of Surface Treated Silicon Dioxide Nanoparticles on Some Mechanical Properties of Maxillofacial Silicone Elastomer,” *International Journal of Biomaterials*, vol. 2014, pp. 1–7, 2014. [Online]. Available: <http://www.hindawi.com/journals/ijbm/2014/750398/>
- [41] A. A. Shamsuri and S. A. A. Z. M. Darius, “Statistical Analysis of Tensile Strength and Flexural Strength Data from Universal Testing Machine,” *Asian Journal of Probability and Statistics*, pp. 54–62, 11 2020.
- [42] Y. Gorash, T. Comlekci, and R. Hamilton, “CAE-Based application for identification and verification of hyperelastic parameters,” *Proceedings of the Institution of Mechanical Engineers, Part L: Journal of Materials: Design and Applications*, vol. 231, no. 7, pp. 611–626, 10 2017. [Online]. Available: <http://journals.sagepub.com/doi/10.1177/1464420715604004>
- [43] Y.-L. Lin, D.-M. Wang, W.-M. Lu, Y.-S. Lin, and K.-L. Tung, “Compression and deformation of soft spherical particles,” *Chemical Engineering Science*, vol. 63, no. 1, pp. 195–203, 1 2008.
- [44] J. Liu, K. Deng, S. Liu, X. Yan, L. Li, D. Zou, and Y. Lin, “Mechanical Behavior and Structure Optimization of Compressed PHP Packer Rubber,” *Journal of Materials Engineering and Performance*, vol. 30, no. 5, pp. 3691–3704, 5 2021.
- [45] T. Li, L. Mu, X. D. Wang, B. Feng, and Z. Y. Jin, “Contact Stress Analysis of Packer Rubber Based on ANSYS Software,” *Advanced Materials Research*, vol. 860–863, pp. 2966–2969, 12 2013.
- [46] A. Vandenbroucke, H. Laurent, N. Ait Hocine, and G. Rio, “A Hyperelasto-Visco-Hysteresis model for an elastomeric behaviour: Experimental and numerical investigations,” *Computational Materials Science*, vol. 48, no. 3, pp. 495–503, 5 2010. [Online]. Available: <https://linkinghub.elsevier.com/retrieve/pii/S092702561000073X>
- [47] K. B. Putra, X. Tian, J. Plott, and A. Shih, “Biaxial test and hyperelastic material models of silicone elastomer fabricated by extrusion-based additive manufacturing for wearable biomedical devices,” *Journal of the Mechanical Behavior of Biomedical Materials*, vol. 107, p. 103733, 7 2020. [Online]. Available: <https://linkinghub.elsevier.com/retrieve/pii/S1751616120302873>
- [48] S. Lagan, A. Chojnacka-Brozek, and A. Liber-Kneć, “FEM Analysis of Hyperelastic Behavior of Pigâs Skin with Anatomical Site Consideration,” 2019, pp. 202–209. [Online]. Available: [http://link.springer.com/10.1007/978-3-319-97286-2\\_18](http://link.springer.com/10.1007/978-3-319-97286-2_18)
- [49] K. Venkatesh Raja and R. Malayalamurthi, “Assessment on assorted hyper-elastic material models applied for large deformation soft finger contact problems,” *International Journal of Mechanics and Materials in Design*, vol. 7, no. 4, pp. 299–305, 12 2011.
- [50] O. H. Yeoh, “Some Forms of the Strain Energy Function for Rubber,” *Rubber Chemistry and Technology*, vol. 66, no. 5, pp. 754–771, 11 1993.
- [51] R. S. Marlow, “A general first-invariant hyperelastic constitutive model,” *Constitutive Models for Rubber III*, pp. 157–160, 2003.
- [52] E. M. Arruda and M. C. Boyce, “A three-dimensional constitutive model for the large stretch behavior of rubber elastic materials,” *Journal of the Mechanics and Physics of Solids*, vol. 41, no. 2, pp. 389–412, 2 1993.

## APPENDIX

### A. Strain energy density (SED) model

The elastic behavior of a typical material can be described by the Young’s modulus and Poisson’s ratio. Elastomers are a type of material that exhibits viscoelastic behavior [24], [25]. The stress-strain response of an elastomer is therefore non-linear and cannot be described by a linear model [24]. A second characteristic of elastomers is that they show elastic behavior at high strain rates [24], [25]. Hyper-elastic materials are a class of materials that allow for 40% or more strain without breaking and plastic deformation [24]. The specimens used allowed high elongation, indicating that Elastic 50A is an elastomeric material. Therefore, a cured structure built with Elastic 50A resin was qualified as a material which can be described with a hyper-elastic material model.

The strain energy function is described by three strain invariants from the Cauchy-Green deformation tensor when assuming isotropy [46]–[49]. The SED-function [25], [47]–[50] is described by

$$W = W(I_1, I_2, I_3). \quad (6)$$

Here, the strain energy density  $W$  is a function of the strain invariants  $I_1, I_2$  and  $I_3$ . The strain invariants [25], [47]–[49] are described by

$$\begin{aligned} I_1 &= \lambda_1^2 + \lambda_2^2 + \lambda_3^2 \\ I_2 &= \lambda_1^2 \lambda_2^2 + \lambda_2^2 \lambda_3^2 + \lambda_3^2 \lambda_1^2 \\ I_3 &= \lambda_1^2 \lambda_2^2 \lambda_3^2 = 1. \end{aligned} \quad (7)$$

Here, the strain invariants  $I_1, I_2$  and  $I_3$  are determined by the principal stresses  $\lambda_1, \lambda_2$  and  $\lambda_3$ . Because incompressibility is assumed, the  $I_3$  term becomes equal to a constant value [28], [50].

Studies by Yildiz, Sheikhi et al., Kunnil et al. and Gorash et al. [24]–[26], [42] used *Ansys Mechanical* for calibration for rubbers or elastomer materials. The models available in *Ansys* assumes that the material is incompressible, isotropic and reversible [42]. Therefore, the calibration of the hyper-elastic material was performed by use of *Ansys Mechanical*.

The calibration is performed by a curve fitting tool. The tool determines the constants of the different SED-functions. The constants are determined by performing a least-square-fit analysis [25], [42]. *Ansys Mechanical* includes the following models for calibration [42], [49]:

- Neo-Hookean
- Arruda-Boyce
- Gent
- Mooney-Rivlin(2, 3, 5, 9 parameter)
- Polynomial form(1st, 2nd, 3rd order)
- Yeoh(1st, 2nd, 3rd order)
- Ogden(1st, 2nd, 3rd order)
- Extended tube

Only models that depend only on the first strain-invariant can be determined by a single uni-axial test [28], [51]. The models that only depend on the first strain-invariant are the Neo-Hookean, the Arruda-Boyce, the Gent and the Yeoh model. The Neo-Hookean

model is only valid for strain-rates up to 30 % [42]. For these reasons, the Arruda-Boyce, the Gent and Yeoh models were selected for the calibration.

The Arruda-Boyce model [52] is described by

$$W = \mu_{ab} \left( \frac{\bar{I}_1 - 3}{2} + \frac{\bar{I}_1^2 - 9}{20\lambda_m^2} + \frac{11(\bar{I}_1^3 - 27)}{1050\lambda_m^4} + \frac{19(\bar{I}_1^4 - 81)}{7000\lambda_m^6} + \frac{519(\bar{I}_1^5 - 243)}{673750\lambda_m^8} \right) \quad (8)$$

Here, the strain energy density  $W$  is determined by the initial shear modulus  $\mu_{ab}$ , the first strain invariant  $I_1$  and the limiting network stretch  $\lambda_m$ . For stability, the limiting network stretch must be equal or higher than one. The Gent model [24] is described by

$$W = -\frac{\mu_g J_m}{2} L_n \left( 1 - \frac{\bar{I}_1 - 3}{J_m} \right) \quad (9)$$

Here, the strain energy density  $W$  is determined by the material constants  $\mu_g$ ,  $J_m$  and the first strain invariant  $I_1$ . There are three different orders of the Yeoh model which can the hyper-elastic behavior. The Yeoh model [26], [50] is described by

$$W = \sum_{i=1}^N C_{i0} (\bar{I}_1 - 3) \quad (10)$$

Here, the strain energy density  $W$  is determined by the material constant  $C$  and the first strain invariant  $I_1$ .

### B. Constants values calibrated for SED-models

Constant	X-Dir	Y-Dir	Z-Dir	
$\mu_{ab}$	1.562E+6	1.044E+6	1.358E+6	Pa
$\lambda_m$	4.245E+7	1.937	2.032	-
$\mu_g$	1.562E+6	0.808E+3	1019	Pa
$J_m$	2.457E+11	0.996	0.989	-
$C_{10,1st}$	7.809E+5	6.940E+5	8.667E+5	Pa
$C_{10,2nd}$	8.082E+5	6.874E+5	8.106E+5	Pa
$C_{20,2nd}$	-2.423E+4	0.481E+3	3.068E+4	Pa
$C_{10,3rd}$	8.788E+5	7.303E+5	8.935E+5	Pa
$C_{20,3rd}$	-2.172E+5	-9.2631E+4	-1.013E+5	Pa
$C_{30,3rd}$	9.640E+5	3.901E+4	3.727E+4	Pa

TABLE VI  
CALIBRATED CONSTANTS HYPER-ELASTIC MODELS